ATLAS CONF Note

ATLAS-CONF-2023-009

13th March 2023

Search for pair-produced Higgsinos decaying via Higgs or Z bosons to final states containing a pair of photons and a pair of b-jets with the ATLAS detector

The ATLAS Collaboration

A search for the pair production of higgsinos $\tilde{\chi}$ in gauge-mediated supersymmetry models, where $\tilde{\chi}$ decays to a light gravitino $\tilde{G}$ either via a Higgs or Z boson, is presented. The search targets final states in which a Higgs boson decays to a photon pair, while the other Higgs or Z boson decays to a $b\bar{b}$ pair, with missing energy associated with the two gravitinos, and it is performed with the ATLAS detector using 139 fb^{-1} of proton–proton collisions at a centre-of-mass energy of $\sqrt{s}$ = 13 TeV. Search regions dependent on the amount of missing energy are defined by the requirements that the di-photon mass should be consistent with the mass of the Higgs boson, and the $b\bar{b}$ mass with the mass of the Higgs or Z boson. The main backgrounds are estimated with data-driven methods using the sidebands of the di-photon mass distribution. No excesses beyond Standard Model expectations are observed and higgsinos with masses up to 320 GeV are excluded, assuming a branching fraction of 100% to $h\tilde{G}$, partly covering a previous gap in sensitivity in this regime.

ATLAS-CONF-2023-009
31 March 2023

In the Minimal Supersymmetric Standard Model [1, 2] two neutral Higgsinos, the proposed spin-half supersymmetric (SUSY) [3] partners of Higgs bosons, mix together with the spin-half partners of the W^0 and the B^0 bosons, forming four neutralino states $\tilde{\chi}^0_{1,2,3,4}$, while the charged Higgsino mixes with the spin-half partners of the $W^\pm$ to form two pairs of chargino states $\tilde{\chi}^\pm_{1,2}$, where indices are ordered in increasing mass. When the mass terms for the spin-half $W^{0,\pm}$ and B^0 partners are large, the most accessible states at colliders are the lightest, Higgsino-dominated, neutralinos $\tilde{\chi}^0_1, \tilde{\chi}^0_2$ and charginos $\tilde{\chi}^\pm_1$. These particles are expected to have a mass around the electroweak scale following naturalness arguments [4, 5], with mass splittings of 1 GeV or less. Such mass spectra are predicted, for example, in gauge-mediated supersymmetry models (GMSB) [6–8] in which the lightest neutralino $\tilde{\chi}^0_1$ is Higgsino dominated and decays to a light gravitino ($\tilde{G}$) [9], the proposed spin-$\frac{3}{2}$ partner of the graviton, in association with a Higgs or Z boson.

These processes represent a rather promising supersymmetry search target at the LHC, particularly if other SUSY particles are sufficiently heavy as to be kinematically inaccessible or to have suppressed cross sections. The resulting gravitinos would not be detected by collider experiments, but their presence could be inferred from momentum imbalance in the direction perpendicular to the beams ($E_{\mathrm{T}}^{\mathrm{miss}}$). The branching fractions $\mathcal{B}(\tilde{\chi}^0_1 \to h\tilde{G})$ and $\mathcal{B}(\tilde{\chi}^0_1 \to Z\tilde{G})$ will depend on the components of the neutralino mixing matrix. In the following, it will be assumed that there are no additional decay modes of the lightest neutralino, i.e. $\mathcal{B}(\tilde{\chi}^0_1 \to h\tilde{G}) + \mathcal{B}(\tilde{\chi}^0_1 \to Z\tilde{G}) = 100\%$. The subsequent decay products of the h and the Z can be detected in a variety of different decay modes.

This paper presents a search for the $\gamma\gamma bb$ decay mode, which also has sensitivity to $h + Z$ through the Z decays to a pair of b-quarks, as shown in Figure 1. The ATLAS collaboration has previously performed searches using events with at least three b-jets [10], and in $h \to \gamma\gamma$ events without requiring the b-jet decay mode of the other boson [11]. CMS has performed several searches in a variety of decay channels [12–14] including in the $\gamma\gamma bb$ process [14]. For the di-Higgs searches, decays to $\gamma\gamma bb$ combine the advantages of excellent mass resolution in $h \to \gamma\gamma$ with the large Higgs boson branching fraction to $b\bar{b}$.

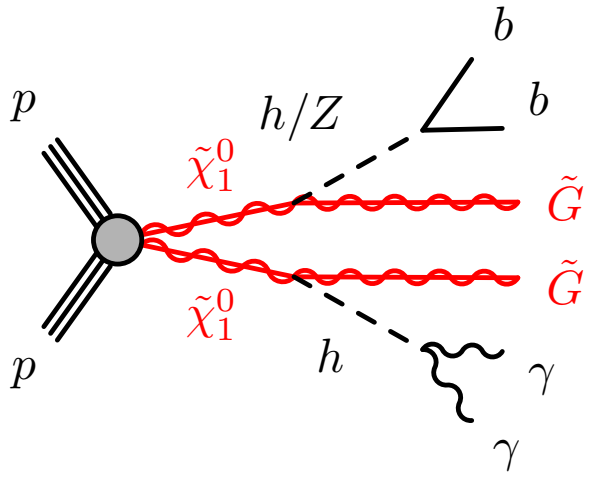

Figure 1: Diagram considered by this search. The diagram shows the production of two neutralinos $\tilde{\chi}^0_1$, which decay to a gravitino $\tilde{G}$ and either a Higgs boson h or a Z boson. This search aims to select events in which a pair of photons is produced by a Higgs boson on one leg of the diagram, while a pair of b-quarks is produced by either the decay of a Higgs boson or a Z boson on the other leg.

The analysis is based on data collected by the ATLAS detector [15] using pp collisions delivered by the LHC [16] between 2015 and 2018, at a centre-of-mass energy of $\sqrt{s} = 13\,\text{TeV}$ with a bunch-crossing interval of 25 ns.

The average number of pp interactions per bunch crossing ranged from about 13 in 2015 to about 39 in 2018. After applying trigger and data-quality requirements [17] the integrated luminosity of the data sample, measured with the LUCID-2 detector [18] using the methods described in Refs. [19, 20], corresponds to $139.0 \pm 2.4\,\text{fb}^{-1}$.

The ATLAS experiment at the LHC is a multipurpose particle detector with a forward–backward symmetric cylindrical geometry and a near 4π coverage in solid angle.[1] It consists of an inner tracking detector surrounded by a thin superconducting solenoid providing a 2 T axial magnetic field, electromagnetic and hadron calorimeters, and a muon spectrometer. The inner tracking detector covers the pseudorapidity range $|\eta| < 2.5$. It consists of silicon pixel, silicon microstrip, and transition radiation tracking detectors. Lead/liquid-argon (LAr) sampling calorimeters provide electromagnetic (EM) energy measurements with high granularity. A steel/scintillator-tile hadron calorimeter covers the central pseudorapidity range ($|\eta| < 1.7$). The endcap and forward regions are instrumented with LAr calorimeters for both the EM and hadronic energy measurements up to $|\eta| = 4.9$. The muon spectrometer surrounds the calorimeters and is based on three large superconducting air-core toroidal magnets with eight coils each. The field integral of the toroids ranges between 2.0 and 6.0 Tm across most of the detector. The muon spectrometer includes a system of precision tracking chambers and fast detectors for triggering. A two-level trigger system is used to select events. The first-level trigger is implemented in hardware and uses a subset of the detector information to accept events at a rate below 100 kHz. This is followed by a software-based trigger that reduces the accepted event rate to 1 kHz on average depending on the data-taking conditions. An extensive software suite [21] is used in data simulation, in the reconstruction and analysis of real and simulated data, in detector operations, and in the trigger and data acquisition systems of the experiment.

For this analysis, photons are reconstructed [22] within pseudorapidity $|\eta| < 2.37$, while vetoing those photons in the EM calorimeter transition region $1.37 < |\eta| < 1.52$ between the calorimeter barrel and endcap, and are requested to have $p_{\text{T}} > 25\,\text{GeV}$. Signal photons are further required to pass `Tight` selection and isolation requirements [22]. Photons with a looser (`Loose'3` [22]) identification and without any isolation requirement, defined as baseline photons, are used to aid the data-driven estimation of some of the backgrounds, as described below.

Jets are reconstructed using the particle-flow algorithm, which combines both calorimeter and tracking information [23]. The anti-k_t algorithm [24] with a radius parameter of $R = 0.4$ is used, with a four-momentum recombination scheme. From the selected jets, b-jets are identified using the DL1 tagger at the 77% efficiency working point, as determined from simulated $t\bar{t}$ events [25].

Electrons are reconstructed from isolated electromagnetic calorimeter energy deposits matched to ID tracks and are required to have $|\eta| < 2.47$, a transverse momentum $p_{\text{T}} > 4.5\,\text{GeV}$, and to satisfy the 'LooseAndBLayer' requirement defined in Ref. [26], which is based on a likelihood using measurements of shower shapes in the calorimeter and track properties in the ID as input variables. Muons are reconstructed in the region $|\eta| < 2.4$ from MS tracks matching ID tracks. They are required to have $p_{\text{T}} > 4\,\text{GeV}$ and

[1] ATLAS uses a right-handed coordinate system with its origin at the nominal interaction point (IP) in the centre of the detector and the z-axis along the beam pipe. The x-axis points from the IP to the centre of the LHC ring, and the y-axis points upward. Cylindrical coordinates (r, ϕ) are used in the transverse plane, ϕ being the azimuthal angle around the z-axis. The pseudorapidity is defined in terms of the polar angle θ as $\eta = -\ln\tan(\theta/2)$.

Table 1: Definition of the three different signal region selections.

requirement	**SR1h**	**SR1Z**	**SR2**
$\lvert m_{\gamma\gamma} - 125\,\text{GeV}\rvert$	$< 5\,\text{GeV}$		
$E_{\text{T}}^{\text{miss}}$	$\leq 100\,\text{GeV}$		$> 100\,\text{GeV}$
m_{bb}	$\in (100, 140)\,\text{GeV}$	$\in (60, 100)\,\text{GeV}$	$\in (35, 145)\,\text{GeV}$
$p_{\text{T}}^{\gamma\gamma}$	$\geq 90\,\text{GeV}$		-
$p_{\text{T}}^{\gamma\gamma}/m_{\gamma\gamma}$	≥ 0.4		≥ 0.2

satisfy the 'medium' identification requirements [27], based on the number of hits in the different ID and MS subsystems, and on the significance of the charge to momentum ratio, q/p.

To avoid reconstruction ambiguities and double counting of analysis objects, electrons, muons and jets are removed from events if they are within $\Delta R = 0.4$ of any photon passing `Loose` identification criteria. While this selection favours photons originating from electron bremsstrahlung over the parent electron itself, such photon candidates do not pass the photon isolation requirements and therefore do not enter the signal regions.

The missing transverse momentum, $E_{\text{T}}^{\text{miss}}$, is constructed [28] from the negative sum of all transverse momenta $-\sum_i p_{\text{T}}^i$ of all reconstructed objects i in the event (photons, jets, muons and electrons, as well as a track soft-term that includes the transverse momenta of all tracks associated with the primary vertex[2] that are not reconstructed as one of the particles listed).

Candidate events are selected using a combination of diphoton triggers [29], and must have exactly two signal photons. To ensure good trigger and reconstruction efficiency the leading (higher p_{T}) photon is required to have $p_{\text{T}} > 35\,\text{GeV}$, and the sub-leading photon to have $p_{\text{T}} > 25\,\text{GeV}$. To reduce the contribution of fake photons the diphoton invariant mass must lie in the range $95\,\text{GeV} < m_{\gamma\gamma} < 160\,\text{GeV}$, and each photon must satisfy $p_{\text{T}}/m_{\gamma\gamma} > 0.2$. Events must have exactly two b-tagged jets, and any event containing one or more reconstructed electrons (with $p_{\text{T}} > 4.5\,\text{GeV}$ and $|\eta| < 2.47$) or muons (with $p_{\text{T}} > 4\,\text{GeV}$ and $|\eta| < 2.7$) is rejected.

Three different signal regions (SR) are then defined (Table 1), to gain sensitivity to different $\tilde{\chi}_1^0$ mass hypotheses and to different decay modes. The three regions are designed to be non-overlapping, allowing a statistical combination which further enhances sensitivity. The SR selections were optimised based on studies of GMSB models with varying $\tilde{\chi}_1^0$ mass, and of differing values of the branching fractions $\mathcal{B}(\tilde{\chi}_1^0 \to h\tilde{G})$ and $\mathcal{B}(\tilde{\chi}_1^0 \to Z\tilde{G})$.

Each of the three SRs requires a diphoton invariant mass $m_{\gamma\gamma}$ consistent at the 5 GeV level with the mass of the observed Higgs boson of 125 GeV [30]. The signal regions differ in their requirements on the invariant mass m_{bb} of the b-tagged jets, and in the requirement on the missing transverse momentum. SR1h targets those events that contain two Higgs bosons, and so has an m_{bb} requirement that is also broadly consistent with m_h. A second region, SR1Z, is designed to select events where m_{bb} is instead consistent with m_Z, thus gaining sensitivity to events in which one $\tilde{\chi}_1^0$ decays to $h\tilde{G}$ and the other to $Z\tilde{G}$. These two regions, SR1h and SR1Z, both target the lower end of the allowed $\tilde{\chi}_1^0$ mass range, a region in which $E_{\text{T}}^{\text{miss}}$ is relatively small with $E_{\text{T}}^{\text{miss}} < 100\,\text{GeV}$. Both regions include an additional selection on the transverse momentum of the diphoton system $p_{\text{T}}^{\gamma\gamma}$, as well as on $p_{\text{T}}^{\gamma\gamma}/m_{\gamma\gamma}$, to improve the signal/background ratio.

[2] The primary vertex is defined to be that with the largest $\sum p_{\text{T}}^2$ of associated tracks.

SR2 targets higher-mass $\tilde{\chi}_1^0$ decays, which consequently demands high missing transverse momentum, $E_{\mathrm{T}}^{\mathrm{miss}} > 100\,\mathrm{GeV}$. The expected yield for these higher-mass models is small, so to enhance sensitivity SR2 has a rather loose selection on m_{bb}, which can admit both Higgs- and Z boson decays. No selection on $p_{\mathrm{T}}^{\gamma\gamma}$ is included to retain more signal events.

Monte Carlo simulations are used to design and optimise the search strategy, for calculating the expected yields of signal events, and as part of the background estimation process.

Prompt diphoton production is simulated with the Sherpa 2.2.4 [31] generator. In this set-up, next-to-leading order (NLO) matrix elements for up to one parton, and leading-order (LO) matrix elements for up to three partons are calculated with the Comix [32] and OpenLoops [33–35] libraries. They are matched with the Sherpa parton shower [36] using the MEPS@NLO prescription [37–40] with a dynamic merging cut [41] of 10 GeV. Photons are required to be isolated according to a smooth-cone isolation criterion [42]. Samples are generated using the NNPDF3.0nnlo PDF set [43], along with the dedicated set of tuned parton-shower parameters developed by the Sherpa authors. The production of Higgs events is modelled using the Powheg Box v2 [44–48] generator at NLO with the NNPDF3.0nlo [43] PDF set. The events are interfaced to Pythia 8.230 [49] using the A14 tune [50] and the NNPDF2.3lo [43] PDF set.

The signal Monte Carlo simulates the production of pairs of Higgsinos through initial production of $(\tilde{\chi}_1^{\pm}, \tilde{\chi}_1^{\pm})$, $(\tilde{\chi}_1^{\pm}, \tilde{\chi}_1^0)$, $(\tilde{\chi}_1^{\pm}, \tilde{\chi}_2^0)$, and $(\tilde{\chi}_1^0, \tilde{\chi}_2^0)$. The $\tilde{\chi}_1^{\pm}$ and $\tilde{\chi}_2^0$ are each assumed to have masses 1 GeV larger than the $\tilde{\chi}_1^0$ and to decay promptly to it and to two soft fermions that are undetected. The mass of the gravitino is set to 1 MeV, and the decays $\tilde{\chi}_1^0 \to h\tilde{G}$ and $\tilde{\chi}_1^0 \to Z\tilde{G}$ are similarly assumed to be prompt. Events are generated from leading-order (LO) matrix elements with up to two extra partons, in the MadGraph5_aMC@NLO 2.9.3 [51] generator interfaced to Pythia 8.245. Events are matched using the CKKW-L prescription [52], with a matching scale set to one quarter of the mass of the pair-produced SUSY particles. Signal cross sections are calculated to NLO in the strong coupling constant, adding the resummation of soft gluon emission at next-to-leading-logarithm accuracy (NLO+NLL) [53–60]. The cross section for $m(\tilde{\chi}_1^0) = 150\,\mathrm{GeV}$ amounts to $3.83 \pm 0.16\,\mathrm{pb}^{-1}$.

The generation of all the simulated event samples includes the effect of multiple interactions in the same and neighbouring bunch crossings (pile-up), modelled by overlaying the simulated hard-scattering event with inelastic proton–proton (pp) events generated with Pythia 8.186 [61] using the NNPDF2.3lo set of parton distribution functions (PDF) [62] and the A3 set of tuned parameters [63].

The various background processes contributing to the signal regions are categorised into two classes: resonant and non-resonant backgrounds.

The resonant backgrounds are those that contain Higgs boson decays to $\gamma\gamma$, and so are expected to have a peak in $m_{\gamma\gamma}$ near m_h. They are subdominant, and are determined from Monte Carlo simulations.

The dominant backgrounds are from non-resonant events, those for which no peak at $m_{\gamma\gamma} \approx m_h$ is expected. They include prompt diphoton events and also those with fewer than two prompt photons which can contribute when other detected particles — most often those associated with jets — are falsely identified as photons. These prompt and fake photon non-resonant contributions to the signal regions are modelled using data-driven techniques, since there is a variety of different ways in which mismeasurements can contribute, not all of which are expected to be well-modelled in Monte Carlo simulations.

The data-driven method used to determine the non-resonant backgrounds is known as the "2×2D sideband method", a technique developed in the context of $H \to \gamma\gamma$ measurements [64], and based on similar techniques used at D0 [65] and CDF [66]. The method makes extensive supporting measurements in data

to improve the accuracy of the predictions from Monte Carlo simulations. An outline of the method is given below, while further details may be found in reference [64].

Control regions are defined selecting events in the diphoton sidebands ($|m_{\gamma\gamma} - 125\,\text{GeV}| > 5\,\text{GeV}$) using baseline photons. The looser requirements provide a large yield both of prompt and fake photons, while remaining unbiased by the photon identification requirements of the triggers. These events are then partitioned into categories, based on the photon *identification* status (tight or not-tight) and the photon *isolation* status (isolated or non-isolated). The partitioning is performed separately for the leading and sub-leading photon candidates, thus providing 16 different observable categories of events.

The expected yields of $\gamma\gamma$, γ-jet, jet-γ and jet-jet events in each region can be expressed separately using the yields obtained selecting baseline photons, the prompt photon identification and isolation efficiencies, the fake-photon mis-identification and -isolation probabilities (fake-factors) and the relevant correlations between the fake-factors. It is assumed, based on previous studies [64], that any photon-photon efficiency correlations, photon-jet efficiency correlations or fake-photon mis-identification correlations are negligible.

A simultaneous likelihood fit constrained by the yields in each of the 16 observable categories is then performed to determine the parameters above, where the prompt photon identification and isolation efficiencies are determined using the diphoton Monte Carlo sample. From the fitted parameters the fractions of $\gamma\gamma$, γ-jet, jet-γ and jet-jet events in the control regions are calculated and applied to the corresponding signal and validation regions (VR) defined below. The key assumption, that the fraction of the events of each of these four types is the same between the control region and the corresponding signal region, is justified by the smooth behaviour in $m_{\gamma\gamma}$ of the non-resonant backgrounds across and between the sidebands, and by the fact that the photon identification and isolation efficiencies do not depend strongly on $m_{\gamma\gamma}$ [67].

Since the background composition is expected to change in regions with different $E_{\text{T}}^{\text{miss}}$ requirements, backgrounds are estimated separately for the low-$E_{\text{T}}^{\text{miss}}$ signal regions SR1h and SR1Z, and for the high-$E_{\text{T}}^{\text{miss}}$ signal region SR2. In order to overcome the limited statistics in the latter, additional supporting measurements in the $m_{\gamma\gamma}$ sidebands in regions defined inverting the $E_{\text{T}}^{\text{miss}}$ and/or the b-jet multiplicity requirements, are also used in conjunction with those closer to SR2, and the final background prediction is obtained extrapolating from such regions with the aid the ABCD method [68].

To test the accuracy of the background prediction, two VRs are defined. These regions have similar kinematic selections to the signal regions, except that they remove the requirement on $m_{\gamma\gamma}$ while they require that m_{bb} be outside the selection band of the corresponding signal region, resulting in negligible signal contamination ($\lesssim 3\,\%$). The two VRs are designed to reflect the same $E_{\text{T}}^{\text{miss}}$ spectra of the SRs, with VR1 requiring $E_{\text{T}}^{\text{miss}} < 100\,\text{GeV}$ and VR2 $E_{\text{T}}^{\text{miss}} > 100\,\text{GeV}$. The background estimation method described above is applied to the VRs in the same fashion as for the SRs, where correction factors for the predicted numbers of $\gamma\gamma$, γ-jet, jet-γ and jet-jet events are determined in the respective CR and applied in both the VR and the SR. A schematic overview of the signal, control- and validation region strategy is shown in Figure 2.

The overall yields and the shapes of the backgrounds in both VRs are found to be well predicted. Distributions of two of the most important kinematic variables are illustrated in Figure 3.

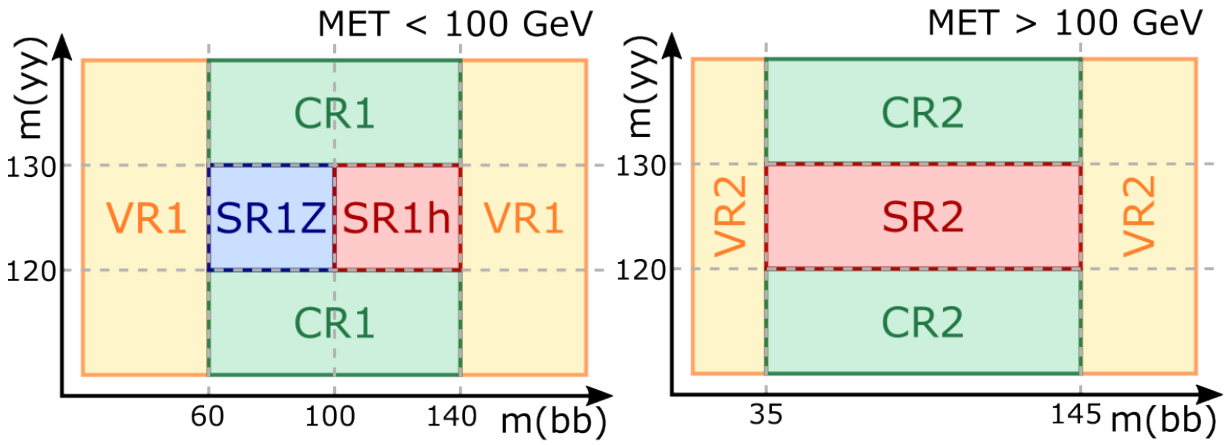

Figure 2: Schematic overview of the event categorisation in this analysis. The control regions (CR) are used to estimate backgrounds. This estimation is applied to both the validation regions (VR) and the signal regions (SR).

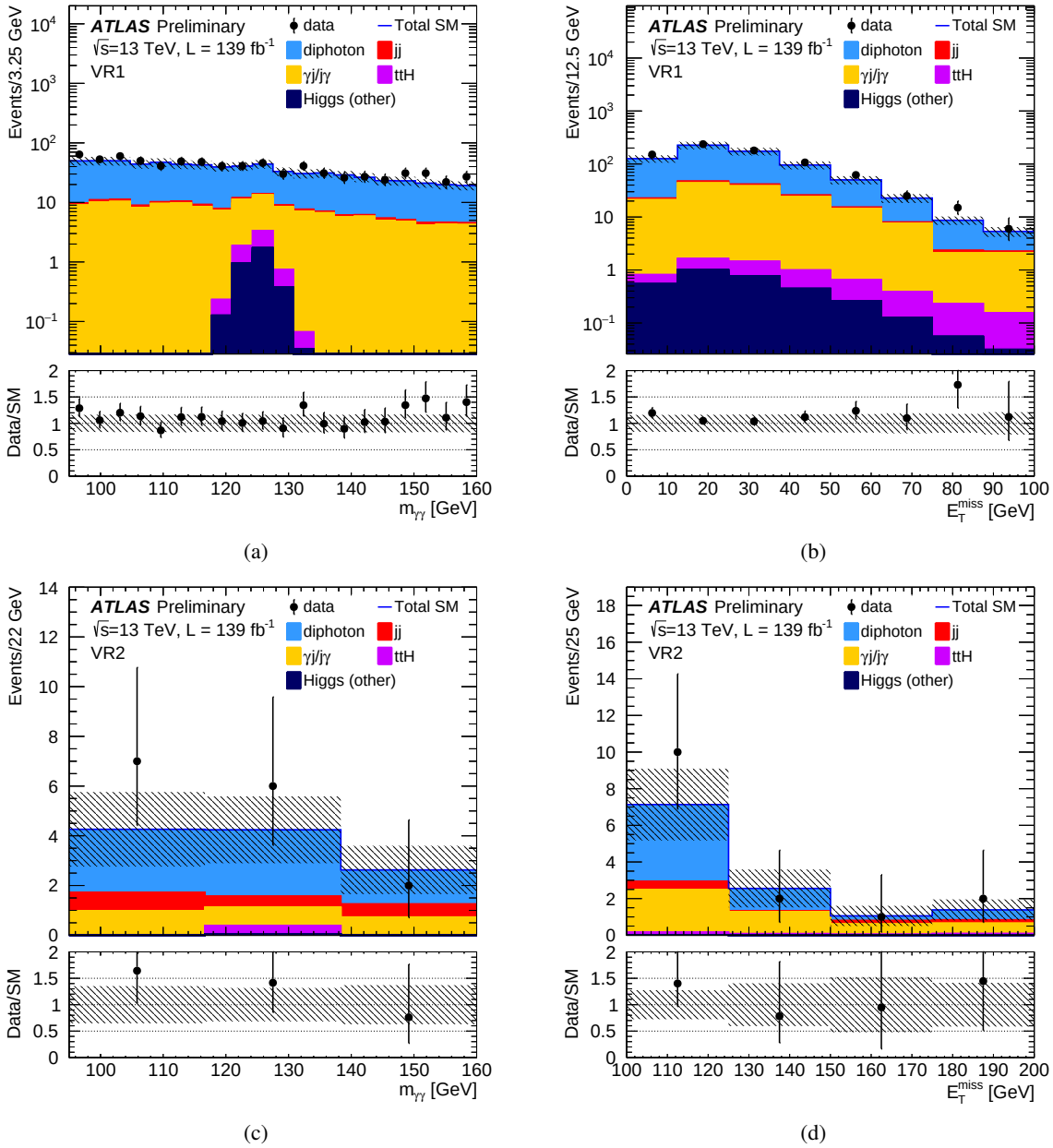

Figure 3: Distribution of the diphoton invariant mass (left) and of the missing transverse momentum (right) in the validation regions VR1 (top) and VR2 (bottom). The solid histograms show the Standard Model expectations after the 2×2D background estimation technique has been applied. Background and signal predictions are normalised to the luminosity. The background category "Higgs (other)" includes events originating from production mechanisms different from ttH, subdominant in this signature. Statistic and systematic uncertainties are indicated by the shaded area. The lower panel of each plot shows the data/SM prediction ratio for the respective bin. The first and last bins include the under- and overflow respectively.

Systematic uncertainties are calculated for three classes of sources: from data-driven background methods, from the modelling of the detector response, from theoretical calculations of different processes that are used to normalise the corresponding MC predictions. The total size of the systematic uncertainty on the prediction for the background yields ranges from 15% to 39%, depending on the signal region. The dominant sources of systematic uncertainty are from the weights calculated by the 2×2D data-driven background method, and from corresponding statistical uncertainty of the associated control regions. Systematic uncertainties associated with the detector response are otherwise found to be negligible. The theoretical uncertainties are found to be at the level of 3% to 6% depending on the SR. The statistical uncertainties are in the range 40% to 77%, depending on the signal region, and so are the dominant source of uncertainty for the available dataset.

The $m_{\gamma\gamma}$ distributions associated with the three signal regions are shown in Figure 4. The observed yields in each SR, reported in Table 2, are found to be consistent with the corresponding Standard Model predictions, and inconsistent with substantial additional contributions from the supersymmetric signal models under test. Table 2 also shows, for each SR, the upper limits (at the 95% CL) on the still possible number of BSM events S^{95}, and on the visible BSM cross section $\langle\epsilon\sigma\rangle^{95}_{\text{obs}} = S^{95}_{\text{obs}}/\int\mathcal{L}\mathrm{d}t$, defined as the product of the production cross section with the ATLAS experimental acceptance and efficiency.

A statistical combination of the three signal regions was performed, and a limit on the predicted cross section for Higgsino pair-production calculated. The results of this statistical combination are shown in Figure 5 for the assumption $\mathcal{B}(\tilde{\chi}^0_1 \to h\tilde{G}) = 100\%$. Under the same assumption, cross sections above 1 pb are excluded at 95% CL for $m(\tilde{\chi}^0_1) < 150\,\text{GeV}$, and the theoretical prediction for the pure Higgsino cross section is excluded at 95% CL for neutralino masses $< 320\,\text{GeV}$.

Relaxing the branching fraction assumption such that the Higgsino may decay either via $\tilde{\chi}^0_1 \to h\tilde{G}$ or via

Table 2: Observed and expected numbers of events in the 3 signal regions. The background category "Higgs (other)" includes events originating from production mechanisms different from ttH, subdominant in this signature. The table also includes model-independent 95% CL upper limits on the visible number of BSM events (S^{95}_{obs}), the number of BSM events given the expected number of background events (S^{95}_{exp}) and the visible BSM cross section ($\langle\epsilon\sigma\rangle^{95}_{\text{obs}}$), all calculated from pseudo-experiments. The discovery p-value (p_0) is also shown and its value is capped at 0.5 if the observed number of events is below the expected number of events.

Channel	SR1h	SR1Z	SR2
Observed events	3	5	2
Total SM events	3.9 ± 0.6	6.4 ± 1.0	1.7 ± 0.7
$\gamma\gamma$ events	2.5 ± 0.5	3.7 ± 0.7	0.88 ± 0.26
γj events	0.47 ± 0.28	0.8 ± 0.5	0.24 ± 0.15
$j\gamma$ events	0.088 ± 0.014	0.27 ± 0.04	0.00 ± 0.6
jj events	< 0.01	0.07 ± 0.05	$0.22^{+0.24}_{-0.22}$
ttH events	0.41 ± 0.04	0.297 ± 0.025	0.27 ± 0.06
Higgs (other)	0.40 ± 0.08	1.22 ± 0.26	0.064 ± 0.011
$\langle\epsilon\sigma\rangle^{95}_{\text{obs}}$ [fb]	0.03	0.04	0.03
S^{95}_{obs}	4.8	5.5	4.8
S^{95}_{exp}	$5.4^{+2.2}_{-1.5}$	$6.7^{+2.6}_{-1.8}$	$4.6^{+1.6}_{-0.8}$
$p(s=0)$	0.50	0.50	0.43

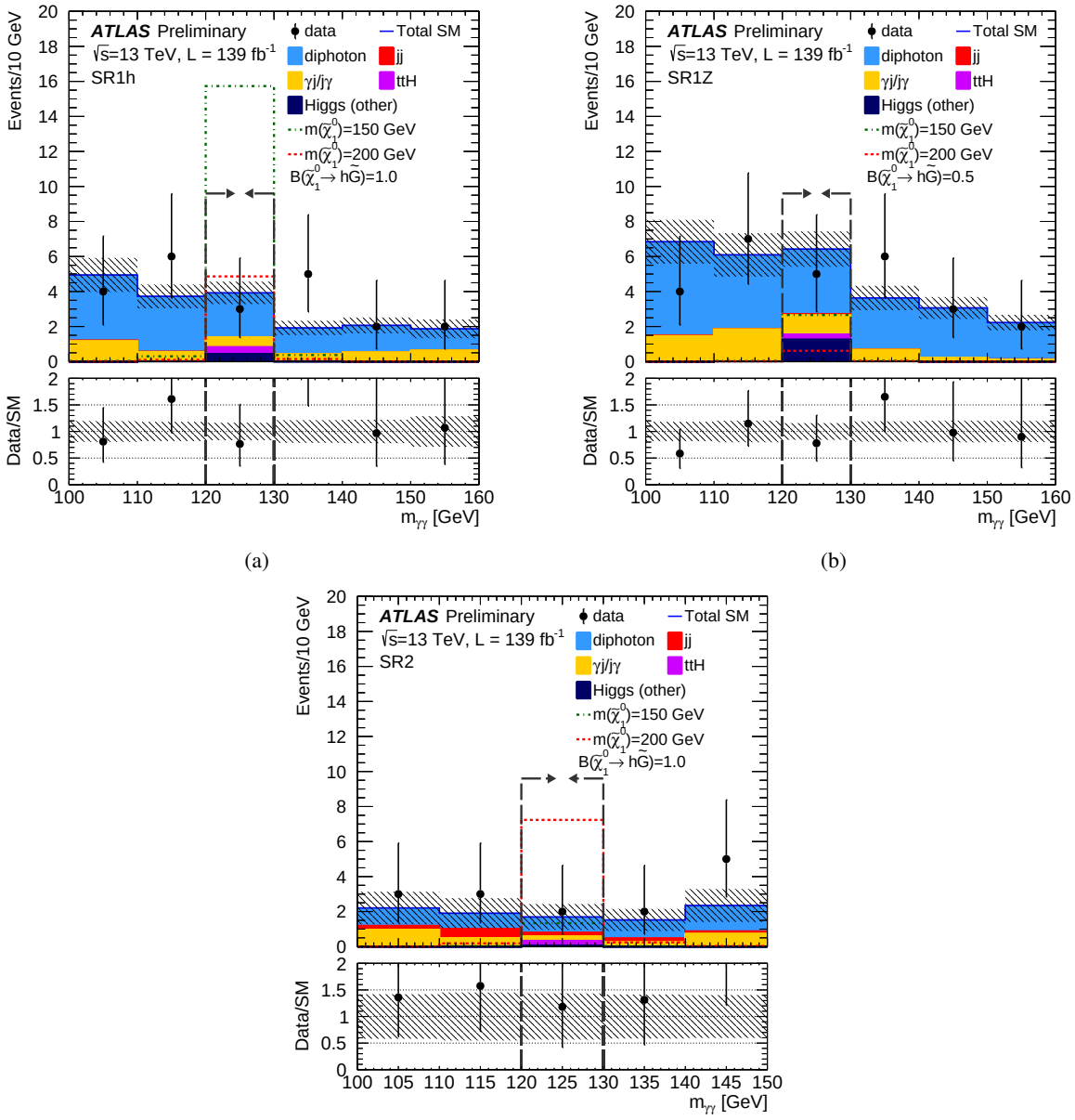

Figure 4: Distribution of the diphoton invariant mass with all selections of the signal regions applied, except on $m_{\gamma\gamma}$ itself, for the three signal regions: SR1h (4(a)), SR1Z (4(b)) and SR2 (4(c)). The background estimation techniques described in the text have been applied. Background and signal predictions are normalised to the luminosity. The background category "Higgs (other)" includes events originating from production mechanisms different from ttH, subdominant in this signature. The sizes of the statistic and systematic uncertainties are indicated by the shaded areas. The lower panel shows the data/SM prediction ratio. Arrows indicate the borders of the signal region ($|m_{\gamma\gamma} - 125\,\text{GeV}| < 5\,\text{GeV}$). The predicted yields for signal benchmark models of varying $\tilde{\chi}_1^0$ mass are also plotted under different assumptions for $\mathcal{B}(\tilde{\chi}_1^0 \to h\tilde{G})$. The first and last bins include the under- and overflow respectively.

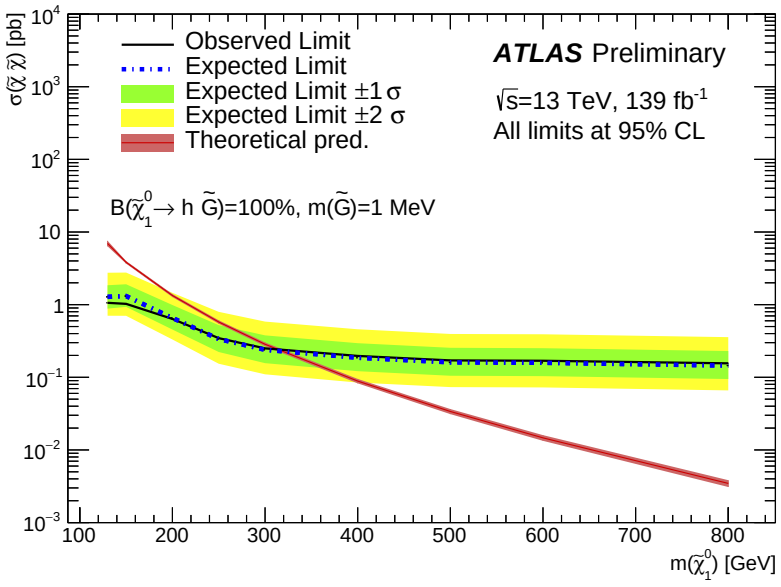

Figure 5: Observed and expected limits on the pure Higgsino cross section at 95% CL assuming $\mathcal{B}(\tilde{\chi}_1^0 \to h\tilde{G}) = 100\%$ for different $\tilde{\chi}_1^0$ masses, obtained by a statistical combination of the three signal regions SR1h, SR1Z and SR2. The green and yellow bands indicate the 1σ and 2σ variation on the expected limit respectively.

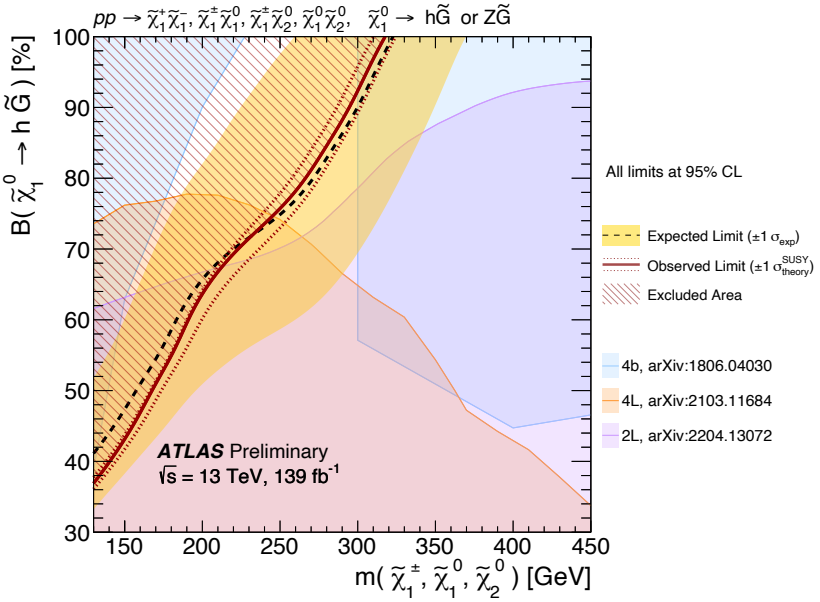

Figure 6: Observed and expected 95% CL limits on the pure-Higgsino branching fraction to $\mathcal{B}(\tilde{\chi}_1^0 \to h\tilde{G})$ against the Higgsino mass $m(\tilde{\chi}_1^0)$ assuming the decays via either $\tilde{\chi}_1^0 \to h\tilde{G}$ or $\tilde{\chi}_1^0 \to Z\tilde{G}$. Limits are shown for different $\tilde{\chi}_1^0$ masses, and are obtained by a statistical combination of the three signal regions SR1h, SR1Z and SR2. The yellow band indicates the $\pm 1\sigma$ variation on the expected limit. The dotted red lines indicate the observed limit obtained by a variation of theoretical prediction for the neutralino production cross section by $\pm 1\,\sigma$. The red shaded area is observed to be excluded by this analysis, while the other coloured areas represent the exclusion reached by complementary ATLAS analyses.

$\tilde{\chi}_1^0 \to Z\tilde{G}$, limits are also set as a function of Higgsino mass and branching fraction, using a statistical combination of the three signal regions. The results of this are shown in Figure 6. As expected, sensitivity is strongest in the region with smaller Higgsino mass, and larger $\mathcal{B}(\tilde{\chi}_1^0 \to h\tilde{G})$. Nevertheless, exclusion at 95% CL extends down to $\mathcal{B}(\tilde{\chi}_1^0 \to h\tilde{G}) = 36\%$ for neutralino masses of 130 GeV.

In conclusion, a search has been performed for excess events containing either pairs of Higgs bosons, or one Higgs boson with one Z boson. The observed data is in agreement with the Standard Model prediction in all three signal regions. A previous ATLAS search optimised for $\mathcal{B}(\tilde{\chi}_1^0 \to h\tilde{G}) = 100\%$ with decays to multiple b-jets did not exclude the region from 250 to 300 GeV due to a $\sim 2\,\sigma$ excess in data [10]. A large fraction of this previously uncovered area is now excluded. The observed 95% CL exclusion is extended up to $m(\tilde{\chi}_1^0) = 320$ GeV for $\mathcal{B}(\tilde{\chi}_1^0 \to h\tilde{G}) = 100\%$ and down to $\mathcal{B}(\tilde{\chi}_1^0 \to h\tilde{G}) = 36\%$ for $m(\tilde{\chi}_1^0) = 130$ GeV.

References

[1] P. Fayet, *Supersymmetry and weak, electromagnetic and strong interactions*, Phys. Lett. B **64** (1976) 159 (cit. on p. 2).

[2] P. Fayet, *Spontaneously broken supersymmetric theories of weak, electromagnetic and strong interactions*, Phys. Lett. B **69** (1977) 489 (cit. on p. 2).

[3] S. P. Martin, *A Supersymmetry Primer*, Adv. Ser. Direct. High Energy Phys. **18** (1998) 1, arXiv: hep-ph/9709356 (cit. on p. 2).

[4] R. Barbieri and G. Giudice, *Upper bounds on supersymmetric particle masses*, Nucl. Phys. B **306** (1988) 63 (cit. on p. 2).

[5] B. de Carlos and J. Casas, *One-loop analysis of the electroweak breaking in supersymmetric models and the fine-tuning problem*, Phys. Lett. B **309** (1993) 320, arXiv: hep-ph/9303291 (cit. on p. 2).

[6] M. Dine and W. Fischler, *A phenomenological model of particle physics based on supersymmetry*, Phys. Lett. B **110** (1982) 227 (cit. on p. 2).

[7] L. Alvarez-Gaumé, M. Claudson and M. B. Wise, *Low-energy supersymmetry*, Nucl. Phys. B **207** (1982) 96 (cit. on p. 2).

[8] C. R. Nappi and B. A. Ovrut, *Supersymmetric extension of the SU(3) x SU(2) x U(1) model*, Phys. Lett. B **113** (1982) 175 (cit. on p. 2).

[9] C. F. Kolda, *Gauge mediated supersymmetry breaking: Introduction, review and update*, Nucl. Phys. B Proc. Suppl. **62** (1998) 266, ed. by M. Cvetic and P. Langacker, arXiv: hep-ph/9707450 (cit. on p. 2).

[10] ATLAS Collaboration, *Search for pair production of higgsinos in final states with at least three b-tagged jets in $\sqrt{s} = 13$ TeV pp collisions using the ATLAS detector*, Phys. Rev. D **98** (2018) 092002, arXiv: 1806.04030 [hep-ex] (cit. on pp. 2, 12).

[11] ATLAS Collaboration, *Search for direct production of electroweakinos in final states with missing transverse momentum and a Higgs boson decaying into photons in pp collisions at $\sqrt{s} = 13$ TeV with the ATLAS detector*, JHEP **10** (2020) 005, arXiv: 2004.10894 [hep-ex] (cit. on p. 2).

[12] CMS Collaboration, *Searches for electroweak neutralino and chargino production in channels with Higgs, Z, and W bosons in pp collisions at 8 TeV*, Phys. Rev. D **90** (2014) 092007, arXiv: 1409.3168 [hep-ex] (cit. on p. 2).

[13] CMS Collaboration, *Search for Higgsino pair production in pp collisions at $\sqrt{s} = 13$ TeV in final states with large missing transverse momentum and two Higgs bosons decaying via $H \to b\bar{b}$*, Phys. Rev. D **97** (2018) 032007, arXiv: 1709.04896 [hep-ex] (cit. on p. 2).

[14] CMS Collaboration, *Search for supersymmetry using Higgs boson to diphoton decays at $\sqrt{s} = 13$ TeV*, JHEP **11** (2019) 109, arXiv: 1908.08500 [hep-ex] (cit. on p. 2).

[15] ATLAS Collaboration, *The ATLAS Experiment at the CERN Large Hadron Collider*, JINST **3** (2008) S08003 (cit. on p. 3).

[16] L. Evans and P. Bryant, *LHC Machine*, JINST **3** (2008) S08001 (cit. on p. 3).

[17] ATLAS Collaboration, *ATLAS data quality operations and performance for 2015–2018 data-taking*, JINST **15** (2020) P04003, arXiv: 1911.04632 [physics.ins-det] (cit. on p. 3).

[18] G. Avoni et al., *The new LUCID-2 detector for luminosity measurement and monitoring in ATLAS*, JINST **13** (2018) P07017 (cit. on p. 3).

[19] ATLAS Collaboration, *Luminosity determination in pp collisions at $\sqrt{s} = 8$ TeV using the ATLAS detector at the LHC*, Eur. Phys. J. C **76** (2016) 653, arXiv: 1608.03953 [hep-ex] (cit. on p. 3).

[20] ATLAS Collaboration, *Luminosity determination in pp collisions at $\sqrt{s} = 13$ TeV using the ATLAS detector at the LHC*, ATLAS-CONF-2019-021, 2019, URL: https://cds.cern.ch/record/2677054 (cit. on p. 3).

[21] ATLAS Collaboration, *The ATLAS Collaboration Software and Firmware*, ATL-SOFT-PUB-2021-001, 2021, URL: https://cds.cern.ch/record/2767187 (cit. on p. 3).

[22] ATLAS Collaboration, *Electron and photon performance measurements with the ATLAS detector using the 2015–2017 LHC proton–proton collision data*, JINST **14** (2019) P12006, arXiv: 1908.00005 [hep-ex] (cit. on p. 3).

[23] ATLAS Collaboration, *Jet reconstruction and performance using particle flow with the ATLAS Detector*, Eur. Phys. J. C **77** (2017) 466, arXiv: 1703.10485 [hep-ex] (cit. on p. 3).

[24] M. Cacciari, G. P. Salam and G. Soyez, *The anti-k_t jet clustering algorithm*, JHEP **04** (2008) 063, arXiv: 0802.1189 [hep-ph] (cit. on p. 3).

[25] ATLAS Collaboration, *ATLAS b-jet identification performance and efficiency measurement with $t\bar{t}$ events in pp collisions at $\sqrt{s} = 13$ TeV*, Eur. Phys. J. C **79** (2019) 970, arXiv: 1907.05120 [hep-ex] (cit. on p. 3).

[26] ATLAS Collaboration, *Electron reconstruction and identification in the ATLAS experiment using the 2015 and 2016 LHC proton–proton collision data at $\sqrt{s} = 13$ TeV*, Eur. Phys. J. C **79** (2019) 639, arXiv: 1902.04655 [hep-ex] (cit. on p. 3).

[27] ATLAS Collaboration, *Muon reconstruction and identification efficiency in ATLAS using the full Run 2 pp collision data set at $\sqrt{s} = 13$ TeV*, Eur. Phys. J. C **81** (2021) 578, arXiv: 2012.00578 [hep-ex] (cit. on p. 4).

[28] ATLAS Collaboration, *Performance of missing transverse momentum reconstruction with the ATLAS detector using proton–proton collisions at* $\sqrt{s} = 13$ *TeV*, Eur. Phys. J. C **78** (2018) 903, arXiv: 1802.08168 [hep-ex] (cit. on p. 4).

[29] ATLAS Collaboration, *Operation of the ATLAS trigger system in Run 2*, JINST **15** (2020) P10004, arXiv: 2007.12539 [hep-ex] (cit. on p. 4).

[30] ATLAS Collaboration, *Measurement of the Higgs boson mass in the* $H \to ZZ^* \to 4\ell$ *decay channel using 139* fb^{-1} *of* $\sqrt{s} = 13$ *TeV* pp *collisions recorded by the ATLAS detector at the LHC*, (2022), arXiv: 2207.00320 [hep-ex] (cit. on p. 4).

[31] E. Bothmann et al., *Event generation with Sherpa 2.2*, SciPost Phys. **7** (2019) 034, arXiv: 1905.09127 [hep-ph] (cit. on p. 5).

[32] T. Gleisberg and S. Höche, *Comix, a new matrix element generator*, JHEP **12** (2008) 039, arXiv: 0808.3674 [hep-ph] (cit. on p. 5).

[33] F. Buccioni et al., *OpenLoops 2*, Eur. Phys. J. C **79** (2019) 866, arXiv: 1907.13071 [hep-ph] (cit. on p. 5).

[34] F. Cascioli, P. Maierhöfer and S. Pozzorini, *Scattering Amplitudes with Open Loops*, Phys. Rev. Lett. **108** (2012) 111601, arXiv: 1111.5206 [hep-ph] (cit. on p. 5).

[35] A. Denner, S. Dittmaier and L. Hofer, *Collier: A fortran-based complex one-loop library in extended regularizations*, Comput. Phys. Commun. **212** (2017) 220, arXiv: 1604.06792 [hep-ph] (cit. on p. 5).

[36] S. Schumann and F. Krauss, *A parton shower algorithm based on Catani–Seymour dipole factorisation*, JHEP **03** (2008) 038, arXiv: 0709.1027 [hep-ph] (cit. on p. 5).

[37] S. Höche, F. Krauss, M. Schönherr and F. Siegert, *A critical appraisal of NLO+PS matching methods*, JHEP **09** (2012) 049, arXiv: 1111.1220 [hep-ph] (cit. on p. 5).

[38] S. Höche, F. Krauss, M. Schönherr and F. Siegert, *QCD matrix elements + parton showers. The NLO case*, JHEP **04** (2013) 027, arXiv: 1207.5030 [hep-ph] (cit. on p. 5).

[39] S. Catani, F. Krauss, B. R. Webber and R. Kuhn, *QCD Matrix Elements + Parton Showers*, JHEP **11** (2001) 063, arXiv: hep-ph/0109231 (cit. on p. 5).

[40] S. Höche, F. Krauss, S. Schumann and F. Siegert, *QCD matrix elements and truncated showers*, JHEP **05** (2009) 053, arXiv: 0903.1219 [hep-ph] (cit. on p. 5).

[41] F. Siegert, *A practical guide to event generation for prompt photon production with Sherpa*, J. Phys. G **44** (2017) 044007, arXiv: 1611.07226 [hep-ph] (cit. on p. 5).

[42] S. Frixione, *Isolated photons in perturbative QCD*, Phys. Lett. B **429** (1998) 369, arXiv: hep-ph/9801442 (cit. on p. 5).

[43] R. D. Ball et al., *Parton distributions for the LHC run II*, JHEP **04** (2015) 040, arXiv: 1410.8849 [hep-ph] (cit. on p. 5).

[44] S. Frixione, G. Ridolfi and P. Nason, *A positive-weight next-to-leading-order Monte Carlo for heavy flavour hadroproduction*, JHEP **09** (2007) 126, arXiv: 0707.3088 [hep-ph] (cit. on p. 5).

[45] P. Nason, *A new method for combining NLO QCD with shower Monte Carlo algorithms*, JHEP **11** (2004) 040, arXiv: hep-ph/0409146 (cit. on p. 5).

[46] S. Frixione, P. Nason and C. Oleari, *Matching NLO QCD computations with parton shower simulations: the POWHEG method*, JHEP **11** (2007) 070, arXiv: 0709.2092 [hep-ph] (cit. on p. 5).

[47] S. Alioli, P. Nason, C. Oleari and E. Re, *A general framework for implementing NLO calculations in shower Monte Carlo programs: the POWHEG BOX*, JHEP **06** (2010) 043, arXiv: 1002.2581 [hep-ph] (cit. on p. 5).

[48] H. B. Hartanto, B. Jäger, L. Reina and D. Wackeroth, *Higgs boson production in association with top quarks in the POWHEG BOX*, Phys. Rev. D **91** (2015) 094003, arXiv: 1501.04498 [hep-ph] (cit. on p. 5).

[49] T. Sjöstrand et al., *An introduction to PYTHIA 8.2*, Comput. Phys. Commun. **191** (2015) 159, arXiv: 1410.3012 [hep-ph] (cit. on p. 5).

[50] ATLAS Collaboration, *ATLAS Pythia 8 tunes to 7 TeV data*, ATL-PHYS-PUB-2014-021, 2014, URL: https://cds.cern.ch/record/1966419 (cit. on p. 5).

[51] J. Alwall et al., *The automated computation of tree-level and next-to-leading order differential cross sections, and their matching to parton shower simulations*, JHEP **07** (2014) 079, arXiv: 1405.0301 [hep-ph] (cit. on p. 5).

[52] L. Lönnblad, *Correcting the Colour-Dipole Cascade Model with Fixed Order Matrix Elements*, JHEP **05** (2002) 046, arXiv: hep-ph/0112284 (cit. on p. 5).

[53] W. Beenakker, R. Höpker, M. Spira and P. Zerwas, *Squark and gluino production at hadron colliders*, Nucl. Phys. B **492** (1997) 51, arXiv: hep-ph/9610490 (cit. on p. 5).

[54] A. Kulesza and L. Motyka, *Threshold Resummation for Squark-Antisquark and Gluino-Pair Production at the LHC*, Phys. Rev. Lett. **102** (2009) 111802, arXiv: 0807.2405 [hep-ph] (cit. on p. 5).

[55] A. Kulesza and L. Motyka, *Soft gluon resummation for the production of gluino-gluino and squark-antisquark pairs at the LHC*, Phys. Rev. D **80** (2009) 095004, arXiv: 0905.4749 [hep-ph] (cit. on p. 5).

[56] W. Beenakker et al., *Soft-gluon resummation for squark and gluino hadroproduction*, JHEP **12** (2009) 041, arXiv: 0909.4418 [hep-ph] (cit. on p. 5).

[57] W. Beenakker et al., *Squark and gluino hadroproduction*, Int. J. Mod. Phys. A **26** (2011) 2637, arXiv: 1105.1110 [hep-ph] (cit. on p. 5).

[58] B. Fuks, M. Klasen, D. R. Lamprea and M. Rothering, *Gaugino production in proton-proton collisions at a center-of-mass energy of 8 TeV*, JHEP **10** (2012) 081, arXiv: 1207.2159 [hep-ph] (cit. on p. 5).

[59] B. Fuks, M. Klasen, D. R. Lamprea and M. Rothering, *Precision predictions for electroweak superpartner production at hadron colliders with RESUMMINO*, Eur. Phys. J. C **73** (2013) 2480, arXiv: 1304.0790 [hep-ph] (cit. on p. 5).

[60] B. Fuks, M. Klasen, D. R. Lamprea and M. Rothering, *Revisiting slepton pair production at the Large Hadron Collider*, JHEP **01** (2014) 168, arXiv: 1310.2621 [hep-ph] (cit. on p. 5).

[61] T. Sjöstrand, S. Mrenna and P. Skands, *A brief introduction to PYTHIA 8.1*, Comput. Phys. Commun. **178** (2008) 852, arXiv: 0710.3820 [hep-ph] (cit. on p. 5).

[62] R. D. Ball et al., *Parton distributions with LHC data*, Nucl. Phys. B **867** (2013) 244, arXiv: 1207.1303 [hep-ph] (cit. on p. 5).

[63] ATLAS Collaboration, *The Pythia 8 A3 tune description of ATLAS minimum bias and inelastic measurements incorporating the Donnachie–Landshoff diffractive model*, ATL-PHYS-PUB-2016-017, 2016, URL: https://cds.cern.ch/record/2206965 (cit. on p. 5).

[64] ATLAS Collaboration, *Measurement of the isolated diphoton cross section in pp collisions at $\sqrt{s} = 7$ TeV with the ATLAS detector*, Phys. Rev. D **85** (2012) 012003, arXiv: 1107.0581 [hep-ex] (cit. on pp. 5, 6).

[65] V. M. Abazov et al., *Measurement of Direct Photon Pair Production Cross Sections in $p\bar{p}$ Collisions at $\sqrt{s} = 1.96$ TeV*, Phys. Lett. B **690** (2010) 108, arXiv: 1002.4917 [hep-ex] (cit. on p. 5).

[66] T. Aaltonen et al., *Measurement of the Cross Section for Prompt Isolated Diphoton Production in $p\bar{p}$ Collisions at $\sqrt{s} = 1.96$ TeV*, Phys. Rev. Lett. **107** (2011) 102003, arXiv: 1106.5123 [hep-ex] (cit. on p. 5).

[67] ATLAS Collaboration, *Measurements of Higgs boson properties in the diphoton decay channel with $36\,fb^{-1}$ of pp collision data at $\sqrt{s} = 13$ TeV with the ATLAS detector*, Phys. Rev. D **98** (2018) 052005, arXiv: 1802.04146 [hep-ex] (cit. on p. 6).

[68] G. Kasieczka, B. Nachman, M. D. Schwartz and D. Shih, *Automating the ABCD method with machine learning*, Phys. Rev. D **103** (2021) 035021, arXiv: 2007.14400 [hep-ph] (cit. on p. 6).